Doppler compensation for cavity-based atom interferometry

Nourshargh, Rustin; Hedges, Sam; Langlois, Mehdi; Bongs, Kai; Holynski, Michael

DOI:
10.1364/OE.449873

Document Version
Publisher's PDF, also known as Version of record

Citation for published version (Harvard):
Nourshargh, R, Hedges, S, Langlois, M, Bongs, K & Holynski, M 2022, 'Doppler compensation for cavity-based atom interferometry', *Optics Express*, vol. 30, no. 17, pp. 30001-30011. https://doi.org/10.1364/OE.449873

Research Article | Vol. 30, No. 17 / 15 Aug 2022 / Optics Express 30001
Optics EXPRESS

Doppler compensation for cavity-based atom interferometry

RUSTIN NOURSHARGH, SAM HEDGES, MEHDI LANGLOIS, KAI BONGS, AND MICHAEL HOLYNSKI*

School of Physics and Astronomy, University of Birmingham, Edgbaston, Birmingham, B15 2TT, UK
*M.Holynski@bham.ac.uk

Abstract: We propose and demonstrate a scheme for Doppler compensated optical cavity enhancement of atom interferometers at significantly increased mode diameters. This overcomes the primary limitations in cavity enhancement for atom interferometry, circumventing the cavity linewidth limit and enabling spatial mode filtering, power enhancement, and a large beam diameter simultaneously. This approach combines a magnified linear cavity with an intracavity Pockels cell. The Pockels cell induces a voltage-controlled birefringence allowing the cavity mode frequencies to follow the Raman lasers as they track gravitationally induced Doppler shifts, removing the dominant limitation of current cavity enhanced systems. A cavity is built to this geometry and shown to simultaneously realise Doppler compensation, a 5.8 ± 0.15 mm$1/e^2$ diameter beam waist and an enhancement factor of >5× at a finesse of 35. Tuneable Gouy phase enables the suppression of higher order spatial modes and the avoidance of regions of instability. Atom interferometers will see increased contrast at extended interferometry times along with power enhancement and the reduction of optical aberrations. This is relevant to power constrained applications in quantum technology, alongside the absolute performance requirements of fundamental science.

1. Introduction

Light-pulse atom interferometry is a technique employing atomic superposition states as a sensitive probe. Laser pulses act as atomic beam splitters, transferring atoms into a superposition of states where they are left to evolve. Further pulses recombine the superposition, and the final atomic state populations serve as an exquisite record of the environment in which they evolved. The samples, clouds of laser cooled atoms, are interrogated to measure quantities such as gravity, accelerations, and rotations [1–5]. The sensitivity of these instruments is maximized when the interrogation pulses are completed with high fidelity. This requires laser beams with a large diameter compared to the cloud size, high intensities, and aberration-free optical wavefronts with the latter being a leading cause of uncertainty [6–10]. Improvements in instrument sensitivity are achieved by increasing the interferometer space-time area. This can be realized through longer interferometry times or increasing the momentum transferred to the atoms. Interferometry time is typically limited by the available free-fall distance [11], and the thermal expansion of the cloud. Momentum transfer is limited by the atom-optic beam splitter fidelity which depends on the homogeneity of the beam profile, and the pulse parameters which are in practice limited by the available laser power [12]. Using an optical cavity to provide resonant power enhancement and spatial mode filtering of the atom interferometry beams offers considerable promise in addressing these challenges. Existing cavity enhanced atom interferometers have demonstrated the exciting potential of the technique, performing cavity enhanced atom interferometry and realising large momentum transfer beam splitter pulses [13–15]. Challenges implementing large cavity modes in a geometrically stable way and Doppler shift limited interrogation times have so far made it

#449873 https://doi.org/10.1364/OE.449873
Journal © 2022 Received 2 Dec 2021; revised 5 Jul 2022; accepted 6 Jul 2022; published 2 Aug 2022

Optics EXPRESS

difficult to deliver on all of the advantages. Overcoming these challenges would allow cavity enhancement to fully benefit atom interferometers, and have the potential to provide significant advantages to a wide range of experiments, including within fundamental physics [16–24] and practical applications [1,25–28].

During the atom interferometry sequence, changes in the atomic cloud velocities due to gravity or photon recoils result in a Doppler shift of the laser frequencies as seen by the atoms. Accurate control of the interferometer phase requires compensation of this shift by chirping the laser frequency. In this work we consider an atom interferometer employing two-photon Raman transitions on the D_2 line of ^{87}Rb, requiring the frequency difference between the two Raman lasers to be chirped at $\alpha_{\text{chirp}} = 25.1\,\text{MHz}\,\text{s}^{-1}$. However, operation within an optical cavity places restrictions on the laser frequencies, with implications for atom interferometry as outlined in the appendix. Whilst multiple input frequencies separated by the cavity free spectral range ν_{FSR} (or multiples thereof) can be resonant simultaneously, standard cavity manipulations, such as changing the cavity length, do not allow the spacing between resonant modes to be adjusted dynamically. As a result the frequencies cannot be simultaneously resonant with the cavity and compensate the Doppler shift at significant free-fall times, limiting the achievable space-time area for cavity enhanced atom interferometry. This has placed limits on the performance of existing cavity enhanced interferometers [14,29,30].

In addition, cavity enhanced atom interferometry with conventional two mirror cavities has been limited by small mode diameters, comparable to the millimeter scale of the atom cloud. This results in dephasing as atoms in the cloud sample different Rabi frequencies at different locations across the cavity mode. This causes a corresponding loss of contrast in the atom interferometer output. In free space atom interferometers a beam to cloud size ratio greater than ten is generally used. Realizing large modes in an optical cavity is a challenging but tractable problem. Recent advancements have yielded a marginally stable cavity with a mode diameter of 1 cm [14] but marginal stability causes higher order mode degeneracy preventing effective spatial mode filtering, one of the key benefits sought through cavity enhancement.

In this work we demonstrate a cavity enhancement scheme enabling Doppler compensation, large mode diameters, and spatial mode filtering. This is achieved through the combination of a magnified linear cavity and an intracavity Pockels cell. This is the first example of a scheme for simultaneously overcoming two of the main limitations in cavity enhanced atom interferometry, limited free-fall times and small mode volumes.

2. Results

Here the magnified geometry and intracavity Pockels cell approach is described and demonstrated. A 12.5× magnification intracavity telescope produces a Gaussian beam with a $1/e^2$ diameter of 5.8 ± 0.15 mm in a geometrically stable configuration whilst also enabling Gouy phase tuning to maximize higher order mode suppression. An intracavity Pockels cell induces voltage controlled birefringence, lifting the degeneracy of orthogonally polarized cavity modes and enabling independent tuning of their resonant frequencies. Agile control of the Pockels cell birefringence allows the cavity resonances to track the interferometry lasers in frequency as they chirp to compensate for Doppler shifts.

2.1. Mode diameter

Producing large mode diameters within a cavity is technically challenging, and generally requires either a long cavity, or results in higher order mode degeneracy and marginal stability. We avoid these problems with an intracavity telescope focused near infinity in a two mirror cavity, as shown in Fig. 1. Planar mirrors were selected due to wider availability, leaving five free parameters which must be optimize. We tackle this in several stages. First, we determined the appropriate focal lengths by simulating cavities with pairs of lenses to determine the magnification required to

Optics EXPRESS

generate a 5 mm mode diameter within L_3. For each pair of lenses, an ABCD-matrix formalism [31] is used to evaluate the mode radius on mirror-2 (m_2) over the space of possible L_1 and L_2. A contour plot similar to Fig. 2 was produced for each combination allowing us to evaluate achievable mode diameters around the centre of the surface of stability. L_3 is fixed at 390 mm as this is the shortest length that will accommodate the vacuum system for which the cavity is designed. The beam is found to be approximately collimated within L_3 for a large range of other cavity parameters due to the large beam diameter on lens f_2. The resulting combination of lenses in the telescope used the longest focal lengths that we were able to accommodate given our other geometric constraints. The minimum length of L_1 was constrained by the requirement that it was able to accommodate a Pockels cell. The overall cavity length was constrained by the limited space between the optical table and the ceiling in which we needed to accommodate the cavity, beam delivery optics and transmission photodiode, on a 1 m long optical rail. With the focal lengths of the lenses set, L_1 practically constrained, and L_3 fixed, the mode parameters can be fine tuned with adjustment of L_2, which by far the most sensitive of any of the parameters. Optimized parameters are found to be $L_3 = 390\,\text{mm}$ and focal lengths $f_1 = 12\,\text{mm}$ and $f_2 = 150\,\text{mm}$.

We achieve a beam waist of $2w = 5.8 \pm 0.15\,\text{mm}$ on m_2, as measured by a CCD on the signal transmitted through this mirror. Around the central set of lens spacings (L_2), this waist is remarkably insensitive to perturbations in the telescope length. A beam diameter fluctuation of 1% would require a change in L_2 of more than 100 μm. The intrinsic stability of this cavity geometry is such that we were able to construct it from standard optomechanics mounted to an aluminium rail.

2.2. Spatial mode filtering

An optical cavity only supports spatial modes with well defined wavefront profiles. By coupling into the fundamental mode of the cavity we are able to exploit this property to filter unwanted spatial modes and achieve flat optical wavefronts. To provide such filtering effectively, the cavity design must avoid frequency degeneracy between higher order modes and the fundamental mode. Otherwise parasitic coupling to these higher orders produces significant wavefront distortion. This can be resolved by tuning the round trip Gouy phase. Higher order spatial modes acquire Gouy phase more rapidly than the fundamental Gaussian mode and have different resonant frequencies. The magnitude of the Gouy phase acquired over a round trip is given by

$$\phi_{p,q} = (p + q + 1)\cos^{-1}(m) \equiv (p + q + 1)\phi \tag{1}$$

for a higher order mode parameterized by indices p, q (e.g. $\text{TEM}_{p,q}$) in terms of the half-trace of the ABCD matrix describing the cavity, m [32].

Higher order mode degeneracy will occur when $\phi_{p,q}$ is close to a rational fraction of π. Adjusting the spacing of the telescope L_2 allows the half-trace m, and hence the Gouy phase, to be tuned freely over the full range. The Gouy phase is tuned to a value reducing higher order mode degeneracy, whilst maintaining only moderate sensitivity to perturbations in length. Cavity parameters which result in degeneracy with the first five higher order modes are shown in Fig. 2 (three contours and the two boundaries of the surface). We select $m = 0.31$ resulting in $\phi \simeq 1.26$ avoiding the degenerate values of $\pi/2$ and $\pi/3$. Equivalent Gouy phase adjustments are possible if the intracavity lenses are replaced by curved mirrors in a folded geometry, reducing round trip loss [30].

2.3. Doppler compensation using the Pockels Effect

Maintaining cavity resonance whilst independently chirping two input laser frequencies is achieved through the use of an intracavity electro-optic crystal. An intracavity Pockels cell induces a voltage controlled birefringence in the cavity, increasing the optical path length in the slow axis with respect to the fast axis. This lifts the degeneracy between the two orthogonally

Optics EXPRESS

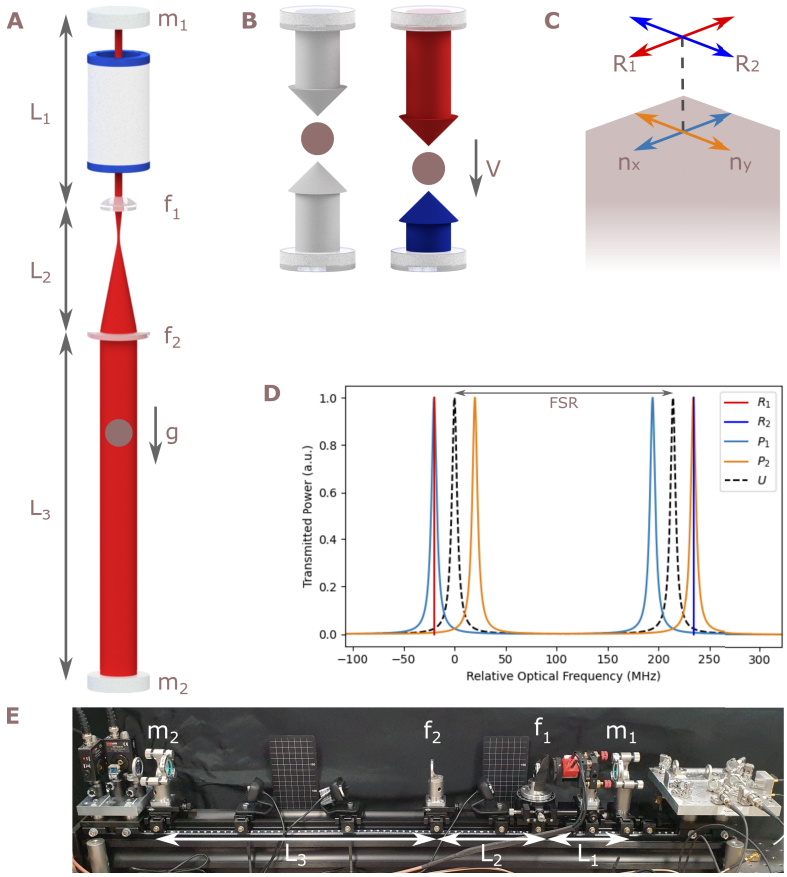

Fig. 1. (A): Schematic overview of the cavity, not to scale. The large mode interaction region is the length L_3. The small waist and in-coupling mode is on mirror m_1 which is planar, as is m_2. The Pockels cell is within L_1. The two lenses have focal lengths $f_1 = 12\,\text{mm}$ and $f_2 = 150\,\text{mm}$ yielding 12.5× magnification. (B): atoms (purple) experience Doppler shifted laser frequencies when moving with respect to the cavity. (C): The linearly polarized Raman beams, R_1 and R_2 are aligned with the orthogonal principle axes of the Pockels cell, n_x and n_y respectively. (D): The Pockels effect enabling tracking of a 40 MHz frequency shift in a simulated cavity with a finesse of 35 and ν_{FSR} of 217 MHz. P_1 and P_2 are the resonant frequencies of the two polarizations within the cavity, which track the chirping Raman lasers R_1 and R_2 in frequency as they compensate for the freefall Doppler shift. U is the uncompensated cavity resonance. (E): A photograph of the completed cavity mounted horizontally for ease of alignment. For atom interferometry the cavity will be orientated vertically with a vacuum chamber positioned within section L_3.

Optics EXPRESS

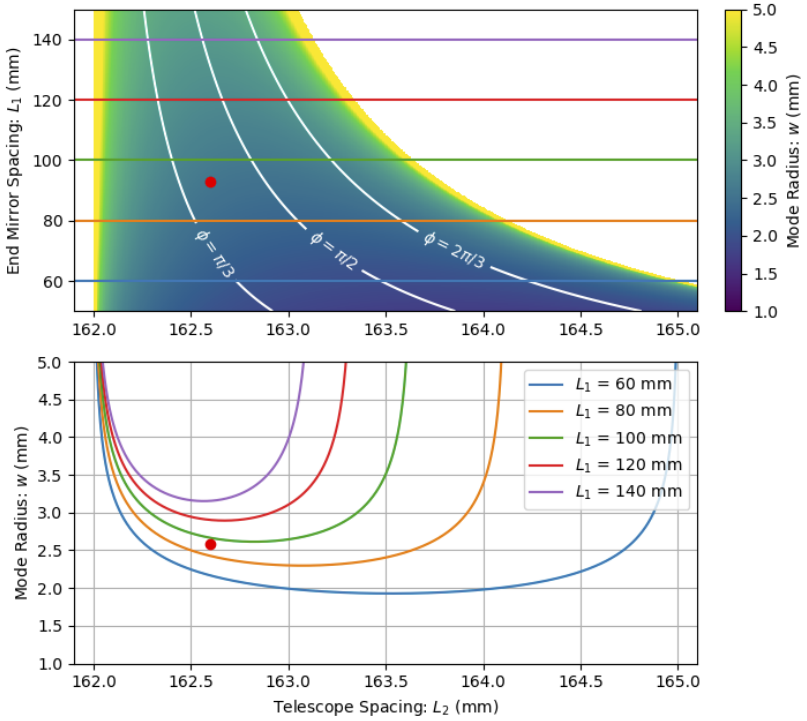

Fig. 2. The design mode radius in the large diameter section of the cavity is shown for different values of L_1 and L_2 in the upper surface plot. At the edges of the surface the radius diverges as the cavity reaches the limits of stability ($m \rightarrow \pm 1$). Specific slices through the surface illustrate the insensitivity of the mode radius to perturbations in L_2; these are shown in the lower plot. In conventional designs with large modes the cavity behaviour is similar to that at the edges of this surface. Owing to the large beam diameter and correspondingly long Rayleigh range, 5.04 mm and 25.6 m respectively, these results are almost completely independent of L_3 which is fixed at $L_3 = 0.39$ m. Contours representing the higher order mode degenerate values of Gouy phase are shown in white, and should be avoided to improve spatial mode performance. The cavity described in this work is indicated by the red spot on each plot. The plot was generated by calculating the ABCD matrices for 10^6 different cavities to select optimal cavity parameters.

Optics EXPRESS

polarized cavity modes and provides a differential shift of their resonant frequencies allowing them to be independently tuned, see Fig. 3. Orthogonal linearly polarized Raman beams implement the atom optics, and the polarization axes are aligned with the principle axes of the Pockels cell, see Fig. 1(C). The frequency shift is linear in applied voltage. An applied birefringence of $\lambda/2$ separates the polarization modes by $\nu_{\mathrm{FSR}}/2$ in a single pass travelling wave cavity and ν_{FSR} in a double pass standing-wave cavity as presented in this work. The slew rate for Doppler compensation is given by

$$\frac{dV}{dt} = \frac{2}{N_{\mathrm{passes}}} \frac{\alpha_{\mathrm{chirp}}}{\nu_{\mathrm{FSR}}} V_{\lambda/2} \tag{2}$$

where the half-wave voltage depends on the Pockels cell crystal, $V_{\lambda/2} = 3.3\,\mathrm{kV}$ for our system, and in the standing wave geometry employed here N_{passes} is two. The required slew rate for Doppler compensation of rubidium in free-fall ($\alpha_{\mathrm{chirp}} = 25.1\,\mathrm{MHz\,s^{-1}}$, $0.4\,\mathrm{kV\,s^{-1}}$ for this cavity), is therefore easily achievable.

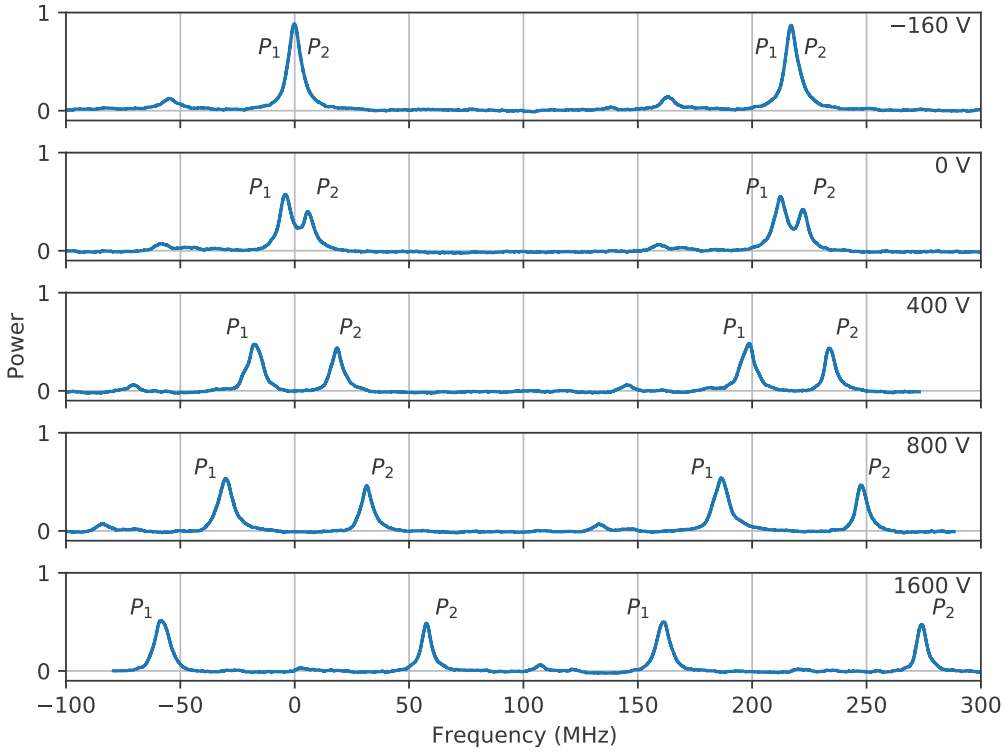

Fig. 3. Increasing the voltage applied to the Pockels cell induces birefringence into the cavity. The orthogonally polarized cavity modes are separated in frequency, from the degenerate value at -160 V to 114 MHz at 1600 V applied. The initial offset compensates for residual birefringence in the crystal. Ramping the voltage at $390\,\mathrm{V\,s^{-1}}$ compensates for the $25.1\,\mathrm{MHz\,s^{-1}}$ Doppler shift.

Pockels cells are bi-polar, meaning that sweeping the voltage from $-V_{\lambda/2} \rightarrow V_{\lambda/2}$ allows the relative frequency to be varied by ν_{FSR} in a travelling wave cavity and $2\nu_{\mathrm{FSR}}$ in a standing wave cavity. If longer sweeps are required, the resonance condition can be maintained by reversing the polarity of the applied voltage between pulses and noting that the longitudinal modes now in use are separated by an additional free spectral range (in a travelling wave configuration a double length Pockels cell is required to achieve arbitrary frequency shifts).

Optics EXPRESS

An intracavity Pockels cell also relaxes the restrictions on cavity lengths. In previous work, fine tuning of the free spectral range ν_{FSR} was required to ensure both Raman beams (separated by the hyperfine frequency splitting ν_{HFS}) are resonant with the cavity simultaneously [13]. This is satisfied when $\nu_{\mathrm{HFS}} = N\nu_{\mathrm{FSR}}$, that is, the frequency splitting between Raman beams is an integer multiple of ν_{FSR}. By allowing the initial Pockels cell voltage to take a non-zero value, resonance can be achieved for both Raman beams without restricting ν_{FSR}. In a system where one of the Raman frequencies is generated by electro-optic modulation, having a non-integer ν_{FSR} separation carries the additional benefit of suppressing any additional frequencies present during the atom interferometry sequence. For instance, for electro-optically generated Raman beams this would suppress unwanted sidebands which would otherwise cause AC-stark shifts and parasitic transitions. Previously such sidebands would have been co-resonant. The degree of suppression will vary as the Pockels cell is scanned and careful choice of pulse timing, cavity ν_{FSR}, and Gouy phase can be used to allow these co-resonances to be avoided.

This technique compensates for Doppler shifts and allows the use of arbitrarily large cavities and at high finesse. The photon lifetime in this cavity is ~ 50 ns, which for typical pulse durations of $1 - 10\ \mu$s will not cause significant temporal pulse distortion. For longer, high finesse cavities with a photon lifetime comparable with the pulse duration, distortion of the temporal profile of the pulses becomes significant and further constraints apply [14,29,33,34].

2.4. Power enhancement

Resonant power enhancement is one of the key benefits we realized with the cavity. This proof of principle system demonstrated a power enhancement of over 5x with a finesse of $\mathcal{F} = 35$, using standard components. This has been achieved despite the cavity mode encountering 26 optical surfaces and passing through intracavity optics. When the vacuum system is added into the cavity for interferometry experiments, the round trip loss will increase by approximately 2% through reflections and transmissive losses from the windows. Whilst modest for a typical cavity, this is a dramatic enhancement in the context of atom interferometry which could further be improved through optimisation of the optical scheme and components.

3. Discussion

We demonstrate a scheme for cavity enhanced atom interferometry that for the first time combines a large mode diameter with the capability to provide Doppler compensation, reduction of wavefront aberration through spatial mode filtering and power enhancement. This overcomes the two key barriers preventing high performance use of cavity enhanced atom interferometry, while realising the two primary benefits. This is achieved while also being robust to changes in cavity length, avoiding the extreme dimensional tolerances encountered at the edges of geometric stability. The techniques described can enable large-mode, high-finesse cavity experiments capable of compensating for arbitrarily large Doppler shifts due to long free-fall times, and the parameters required to enable large momentum transfer orders. Furthermore, this scheme could be applied to state-of-the-art long baseline atom interferometers, with 10 m baselines and 2 s freefall times [35], while still remaining within the limitations imposed by cavity lifetime elongation [29]. As such, this scheme is highly applicable to the full range of applications for atom interferometry. For fundamental physics, the scheme could be applied to realize increased optical intensities and reductions in wave-front aberration to enhance space-time area through large momentum transfer without imposing limitations on free-fall time. For quantum technology sensors the scheme could provide reductions in the required laser power, leading to cheaper sensors or operation on power constrained platforms such as satellites, while also providing a route to increased sensitivity through robust cavity enhancement for large momentum transfer.

Optics EXPRESS

Appendix

Cavity linewidth limit

Atoms in an atom interferometer aligned with gravity experience Doppler shifted laser frequencies during freefall. Chirping the lasers to compensate for the resulting Doppler shift has the undesired effect of moving both laser frequencies away from cavity resonance. This cavity linewidth limit results in reduced circulating intensity and prevents beam splitters entirely at long T times. We arbitrarily define a maximum interrogation time $T_{\max}$, at which the Doppler shift has reduced the circulating intensity to half of it's resonant value for the final beam splitter pulse ($2T_{\max}$ total free fall).

$$T_{\max} = \frac{1}{2}\frac{\nu_{\mathrm{FSR}}}{\alpha_{\mathrm{chirp}}\mathcal{F}} = \frac{1}{2}\frac{c}{\alpha_{\mathrm{chirp}}L_{RT}\mathcal{F}}. \tag{3}$$

The free spectral range of the cavity is ν_{FSR}, α_{chirp} is the chirp rate, $\mathcal{F}$ is the finesse, and L_{RT} is the round trip optical path length of the cavity, twice its physical length for standing wave geometries. At $T_{\max}$ the Rabi frequency is reduced by a factor of two. Beam splitter pulses at this Doppler shift must be twice as long as on resonance and the velocity class that can be addressed is also reduced by a factor of two. The sensitivity of circulating intensity to perturbations in laser frequency or cavity length are all dramatically increased as the laser moves off of resonance. The first order insensitivity on resonance is replaced by the steep gradient of the Lorentzian Cavity transmission function [32].

Pockels Cell

The Pockels cell used is a Gooch and Housego Light Gate 3 BBO Pockels cell, AR coated at 780 nm [36].

Laser system

Light at 780 nm, resonant with the D2 line of rubidium-87, is generated in fiber by frequency doubling a 1560 nm telecoms laser as shown in Fig. 4(A). The output from the 1560 nm seed, a Koheras BASIK E15 from NKT, is split into two arms for the two Raman frequencies. One of the arms is also used to stabilize the laser to the cavity using the Pound-Drever-Hall (PDH) technique. In both arms light travels through an electro-optic modulator (EOM), MPZ-LN-10 from iXblue, is amplified by an Erbium-doped fiber amplifier (EDFA), a CEFA-C-PB from Keopsys, frequency doubled by a quasi-phase matched Lithium-Niobate waveguide for second harmonic generation (SHG), WH-0780 from NTT Electronics, and modulated using an acousto-optic modulator (AOM), MT110-NIR20 from AA Opto-Electronic, before passing through an OZ Optics optical isolator to a fiber collimator where the light is coupled into free space.

The EOM on the arm not locked to the cavity is modulated at $\nu_{\mathrm{HFS}} = 6.835\,\mathrm{GHz}$; the ground state hyperfine splitting in rubidium 87. To produce this a 7 GHz clock is mixed with 164 MHz from an ARTIQ DDS channel using a single sideband mixer achieving 32.7 dB carrier suppression. The RF signals for the remaining EOM and AOMs are supplied by other ARTIQ DDS channels and an arbitrary function generator.

Locking

As we inject light into both cavity polarizations, the standard locking scheme using a polarizing beamsplitter and a $\lambda/4$ (quarter-wave plate) to separate the incident and reflected beams to be sampled for PDH stabilization is not viable [37]. Instead we insert a 5% beam sampler into one of the two polarization beam paths, and stabilize the laser frequency on the sampled fraction of the light reflected from the cavity with standard PDH. This loop is run continuously at low optical power and a large detunig to maintain laser lock whilst minimizing spontaneous emission. The laser is pulsed to full power for the Raman pulses. Adding a sampler and photodiode to the

Optics EXPRESS

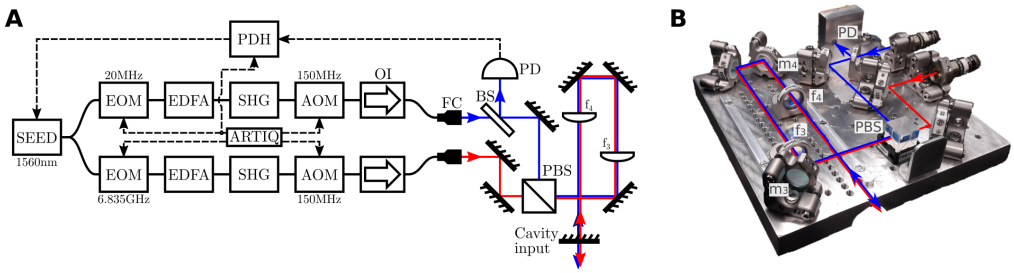

Fig. 4. (A): Laser system schematic. Light at 780 nm is produced by amplifying and frequency doubling a 1560 nm seed. (B): Cavity beam delivery board. Mirrors overlap orthogonal linear polarized light from two fiber collimators. The light is reflected through a mode matching telescope and mirrors m_3 and m_4 are used to achieve spatial overlap with the cavity mode. The cavity reflected light from the polarization shown in blue is reflected by a 5 % beam sampler onto a bespoke photodiode for locking using the Pound-Drever-Hall technique.

second polarization would allow the Pockels cell voltage to be actively stabilized rather than the existing open-loop configuration.

Stabilization of this cavity with an additional wavelength (e.g 1560 nm [15]) is also possible but it would be challenging to implement. The tunable birefringence from the Pockels cell will induce approximately half the phase shift at 1560 nm as that observed at 780 nm with a small additional factor caused by dispersion. Maintaining resonance for a laser at 1560 nm will cause the 780 nm interferometry beams to move off of the cavity resonance unless an additional correction can be applied to compensate for these Pockels cell voltage dependent effects. This would require a significantly increase in feedback loop complexity, likely requiring additional frequency control and a digital feedback loop synchronized with the Pockels cell voltage.

Cavity mode matching

Efficient mode matching is achieved by producing good spatial overlap between the input beam and the cavity mode. We designed a custom beam delivery board to overlap the two laser polarizations on a polarizing beamsplitter, before passing through a telescope, f_3 and f_4 on Fig. 4 to produce a mode of the correct size on the input mirror. Mechanical slides allow the telescope lenses to be translated along the optical axis without introducing tilt or transverse misalignments. The input diameter and location is measured with a CCD which we are able to translate along the cavity rail around the location of the input mirror (removed for this procedure). The telescope lenses are adjusted until the target diameter, determined analytically, is achieved.

Spatial overlap with the cavity mode is attained with a final mirror pair on the delivery board m_3 and m_4. These mirrors are adjusted to maximize coupling to the fundamental mode (and minimize coupling to higher orders) as observed on the cavity transmission photodiode (see Fig. 3). Precise adjustment of these optics allows mode matching efficiencies above 90% before adding the Pockels cell.

Optics alignment

Despite the large number of optics present in this cavity, optical alignment is relatively straightforward. Beginning with an optic axis parallel to the rail, optics are added in turn and adjusted to overlap back reflections with the input beams, see Fig. 1(A). Coarse spacing is measured with mm-level precision, and the critical telescope spacing is adjusted with a micrometer stage to deliver the target beam size from the fixed input, as measured at the waist of the large mode

Optics EXPRESS

region. Retro reflection from m_4 in the absence of m_3 allows the orientation of m_4 to be precisely defined. m_3 is then added, and coarsely aligned by making similar adjustments. Final adjustments should be completed by optimizing the transmission signal. The Pockels cell requires a well centered beam and accurate alignment of roll, tip and tilt, carried out once the cavity is fully aligned. The coarse alignment procedure follows that of standard q-switching applications [36], whilst the final fine tuning is best achieved by supplying a triangle wave voltage to the cell and adjusting the Pockels cell tip and tilt to minimize voltage induced coupling to higher order modes as observed on the cavity transmission. Temporarily adding a half waveplate on the input to the cavity simplifies precise roll alignment, and enables projection of a single input polarization on both crystal axis for alignment purposes. When the crystal axis is aligned with the cavity axis, the applied voltage induces birefringence, splitting the transmission peak in two and increasing this separation with increased voltage, see Fig. 3. The appearance of other peaks or variations in peak amplitude both indicate misalignment.

Funding. Engineering and Physical Sciences Research Council (EP/T001046/1) as part of the UK National Quantum Technologies Programme.

Acknowledgments. The authors thank Camron Nourshargh, Farzad Hayati, and Luuk Earl for their contributions.

Disclosures. The authors declare no conflicts of interest.

Data availability. Data underlying the results presented in this paper are not publicly available at this time but may be obtained from the authors upon reasonable request.

References

1. K. Bongs, M. Holynski, J. Vovrosh, P. Bouyer, G. Condon, E. Rasel, C. Schubert, W. P. Schleich, and A. Roura, "Taking atom interferometric quantum sensors from the laboratory to real-world applications," Nat. Rev. Phys. **1**(12), 731–739 (2019).
2. C. Freier, M. Hauth, V. Schkolnik, B. Leykauf, M. Schilling, H. Wziontek, H.-G. Scherneck, J. Müller, and A. Peters, "Mobile quantum gravity sensor with unprecedented stability," J. Phys.: Conf. Ser. **723**, 012050 (2016).
3. B. Barrett, R. Geiger, I. Dutta, M. Meunier, B. Canuel, A. Gauguet, P. Bouyer, and A. Landragin, "The Sagnac effect: 20 years of development in matter-wave interferometry," C. R. Phys. **15**(10), 875–883 (2014).
4. D. Budker and M. Romalis, "Optical magnetometry," Nat. Phys. **3**(4), 227–234 (2007).
5. S. Bize, "The unit of time: Present and future directions," C. R. Phys. **20**(1-2), 153–168 (2019).
6. A. Trimeche, M. Langlois, S. Merlet, and F. Pereira Dos Santos, "Active control of laser wavefronts in atom interferometers," Phys. Rev. Appl. **7**(3), 034016 (2017).
7. R. Karcher, A. Imanaliev, S. Merlet, and F. P. Dos Santos, "Improving the accuracy of atom interferometers with ultracold sources," New J. Phys. **20**(11), 113041 (2018).
8. M.-K. Zhou, Q. Luo, L.-L. Chen, X.-C. Duan, and Z.-K. Hu, "Observing the effect of wave-front aberrations in an atom interferometer by modulating the diameter of Raman beams," Phys. Rev. A **93**(4), 043610 (2016).
9. V. Schkolnik, B. Leykauf, M. Hauth, C. Freier, and A. Peters, "The effect of wavefront aberrations in atom interferometry," Appl. Phys. B **120**(2), 311–316 (2015).
10. J. M. Hogan, D. M. Johnson, S. Dickerson, T. Kovachy, A. Sugarbaker, S.-w. Chiow, P. W. Graham, M. A. Kasevich, B. Saif, S. Rajendran, P. Bouyer, B. D. Seery, L. Feinberg, and R. Keski-Kuha, "An atomic gravitational wave interferometric sensor in low earth orbit (AGIS-LEO)," Gen. Relativ. Gravit. **43**(7), 1953–2009 (2011).
11. L. Zhou, Z. Y. Xiong, W. Yang, B. Tang, W. C. Peng, K. Hao, R. B. Li, M. Liu, J. Wang, and M. S. Zhan, "Development of an atom gravimeter and status of the 10-meter atom interferometer for precision gravity measurement," Gen. Relativ. Gravit. **43**(7), 1931–1942 (2011).
12. S. wey Chiow, T. Kovachy, J. M. Hogan, and M. A. Kasevich, "Generation of 43 W of quasi-continuous 780 nm laser light via high-efficiency, single-pass frequency doubling in periodically poled lithium niobate crystals," Opt. Lett. **37**(18), 3861–3863 (2012).
13. P. Hamilton, M. Jaffe, J. M. Brown, L. Maisenbacher, B. Estey, and H. Müller, "Atom interferometry in an optical cavity," Phys. Rev. Lett. **114**(10), 100405 (2015).
14. I. Riou, N. Mielec, G. Lefèvre, M. Prevedelli, A. Landragin, P. Bouyer, A. Bertoldi, R. Geiger, and B. Canuel, "A marginally stable optical resonator for enhanced atom interferometry," J. Phys. B: At., Mol. Opt. Phys. **50**(15), 155002 (2017).
15. D. Sabulsky, J. Junca, X. Zou, A. Bertoldi, M. Prevedelli, Q. Beaufils, R. Geiger, A. Landragin, P. Bouyer, and B. Canuel, "Multi-photon atom interferometry via cavity-enhanced bragg diffraction," arXiv preprint arXiv:2201.11693 (2022).
16. P. W. Graham, J. M. Hogan, M. A. Kasevich, S. Rajendran, and R. W. Romani, "Mid-band gravitational wave detection with precision atomic sensors," arXiv preprint arXiv:1711.02225 (2017).

Optics EXPRESS

17. L. Badurina, E. Bentine, D. Blas, K. Bongs, D. Bortoletto, T. Bowcock, K. Bridges, W. Bowden, O. Buchmueller, C. Burrage, J. Coleman, G. Elertas, J. Ellis, C. Foot, V. Gibson, M. G. Haehnelt, T. Harte, S. Hedges, R. Hobson, M. Holynski, T. Jones, M. Langlois, S. Lellouch, M. Lewicki, R. Maiolino, P. Majewski, S. Malik, J. March-Russell, C. McCabe, D. Newbold, B. Sauer, U. Schneider, I. Shipsey, Y. Singh, M. A. Uchida, T. Valenzuela, M. van der Grinten, V. Vaskonen, J. Vossebeld, D. Weatherill, and I. Wilmut, "AION: an atom interferometer observatory and network," J. Cosmol. Astropart. Phys. **2020**(05), 011 (2020).
18. D. O. Sabulsky, I. Dutta, E. A. Hinds, B. Elder, C. Burrage, and E. J. Copeland, "Experiment to detect dark energy forces using atom interferometry," Phys. Rev. Lett. **123**(6), 061102 (2019).
19. G. Lamporesi, A. Bertoldi, L. Cacciapuoti, M. Prevedelli, and G. M. Tino, "Determination of the Newtonian gravitational constant using atom interferometry," Phys. Rev. Lett. **100**(5), 050801 (2008).
20. R. H. Parker, C. Yu, W. Zhong, B. Estey, and H. Müller, "Measurement of the fine-structure constant as a test of the Standard Model," Science **360**(6385), 191–195 (2018).
21. C. Overstreet, P. Asenbaum, T. Kovachy, R. Notermans, J. M. Hogan, and M. A. Kasevich, "Effective inertial frame in an atom interferometric test of the equivalence principle," Phys. Rev. Lett. **120**(18), 183604 (2018).
22. P. Asenbaum, C. Overstreet, M. Kim, J. Curti, and M. A. Kasevich, "Atom-interferometric test of the equivalence principle at the 10^{-12} level," Phys. Rev. Lett. **125**(19), 191101 (2020).
23. S. Dimopoulos, P. W. Graham, J. M. Hogan, M. A. Kasevich, and S. Rajendran, "Atomic gravitational wave interferometric sensor," Phys. Rev. D **78**(12), 122002 (2008).
24. M. Jaffe, P. Haslinger, V. Xu, P. Hamilton, A. Upadhye, B. Elder, J. Khoury, and H. Müller, "Testing sub-gravitational forces on atoms from a miniature in-vacuum source mass," Nat. Phys. **13**(10), 938–942 (2017).
25. X. Wu, Z. Pagel, B. S. Malek, T. H. Nguyen, F. Zi, D. S. Scheirer, and H. Müller, "Gravity surveys using a mobile atom interferometer," Sci. Adv. **5**(9), eaax0800 (2019).
26. A. Hinton, M. Perea-Ortiz, J. Winch, J. Briggs, S. Freer, D. Moustoukas, S. Powell-Gill, C. Squire, A. Lamb, C. Rammeloo, B. Stray, G. Voulazeris, L. Zhu, A. Kaushik, Y.-H. Lien, A. Niggebaum, A. Rodgers, A. Stabrawa, D. Boddice, S. R. Plant, G. W. Tuckwell, K. Bongs, N. Metje, and M. Holynski, "A portable magneto-optical trap with prospects for atom interferometry in civil engineering," Philos. Trans. R. Soc., A **375**(2099), 20160238 (2017).
27. Y. Bidel, N. Zahzam, A. Bresson, C. Blanchard, M. Cadoret, A. V. Olesen, and R. Forsberg, "Absolute airborne gravimetry with a cold atom sensor," J. Geod. **94**(2), 20 (2020).
28. B. Stray, A. Lamb, A. Kaushik, J. Vovrosh, A. Rodgers, J. Winch, F. Hayati, D. Boddice, A. Stabrawa, A. Niggebaum, M. Langlois, Y.-H. Lien, S. Lellouch, S. Roshanmanesh, K. Ridley, G. de Villiers, G. Brown, T. Cross, G. Tuckwell, A. Faramarzi, N. Metje, K. Bongs, and M. Holynski, "Quantum sensing for gravity cartography," Nature **602**(7898), 590–594 (2022).
29. M. Dovale-Álvarez, D. D. Brown, A. W. Jones, C. M. Mow-Lowry, H. Miao, and A. Freise, "Fundamental limitations of cavity-assisted atom interferometry," Phys. Rev. A **96**(5), 053820 (2017).
30. M. D. Álvarez, *Optical cavities for optical atomic clocks, atom interferometry and gravitational-wave detection* (Springer, 2019).
31. H. Kogelnik and T. Li, "Laser beams and resonators," Appl. Opt. **5**(10), 1550–1567 (1966).
32. A. Siegman, *Lasers* (University Science Books, 1986).
33. R. Nourshargh, S. Lellouch, S. Hedges, M. Langlois, K. Bongs, and M. Holynski, "Circulating pulse cavity enhancement as a method for extreme momentum transfer atom interferometry," Commun. Phys. **4**(1), 257 (2021).
34. A. Bertoldi, C.-H. Feng, D. S. Naik, B. Canuel, P. Bouyer, and M. Prevedelli, "Fast control of atom-light interaction in a narrow linewidth cavity," Phys. Rev. Lett. **127**(1), 013202 (2021).
35. S. M. Dickerson, J. M. Hogan, A. Sugarbaker, D. M. S. Johnson, and M. A. Kasevich, "Multiaxis inertial sensing with long-time point source atom interferometry," Phys. Rev. Lett. **111**(8), 083001 (2013).
36. G. Ohio, "Pockels cell alignment for single pass systems," (2012).
37. E. D. Black, "An introduction to Pound–Drever–Hall laser frequency stabilization," Am. J. Phys. **69**(1), 79–87 (2001).